Applied Energy 260 (2020) 114291

Contents lists available at ScienceDirect

Applied Energy

journal homepage: www.elsevier.com/locate/apenergy

Local degradation effects in automotive size membrane electrode assemblies under realistic operating conditions

Tim Lochner[a,b,*], Laurens Hallitzky[a], Markus Perchthaler[a], Michael Obermaier[a], Jarek Sabawa[a,b], Simon Enz[a], Aliaksandr S. Bandarenka[b,c,*]

[a] BMW Group, 80809 München, Germany
[b] Physik-Department ECS, Technische Universität München, James-Franck-Str. 1, D-85748 Garching, Germany
[c] Catalysis Research Center, Technical University of Munich, Ernst-Otto-Fischer-Str. 1, 85748 Garching, Germany

HIGHLIGHTS

- An automotive size single cell was operated under automotive operational parameter sets.
- The current density distribution was dominated by the partial pressure of H_2 due to flooding of the anode catalyst layer.
- Optimization of the flow field plays a key role in avoiding flooding of the anode.

GRAPHICAL ABSTRACT

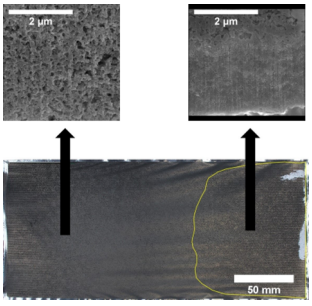

ARTICLE INFO

Keywords:
PEMFC
Automotive size
Fuel starvation
Local current
Local humidity
Degradation

ABSTRACT

In automotive applications, the operational parameters for fuel cell (FC) systems can vary over a wide range. To analyze their impact on fuel cell degradation, an automotive size single cell was operated under realistic working conditions. The parameter sets were extracted from the FC system modeling based on on-road customer data. The parameter variation included simultaneous variation of the FC load, gas pressures, cell temperature, stoichiometries and relative humidity. Current density distributions and the overall cell voltage were recorded in real time during the tests. The current densities were low at the geometric anode gas outlet and high at the anode gas inlet. After electrochemical tests, post mortem analysis was conducted on the membrane electrode assemblies using scanning electron microscopy. The *ex-situ* analysis showed significant cathode carbon corrosion in areas associated with low current densities. This suggests that fuel starvation close to the anode outlet is the origin of the cathode electrode degradation. The results of the numerical simulations reveal high relative humidity at that region and, therefore, water flooding is assumed to cause local anode fuel starvation. Even though the hydrogen oxidation reaction has low kinetic overpotentials, "local availability" of H_2 plays a significant role in maintaining a homogeneous current density distribution and thereby in local degradation of the cathode catalyst layer. The described phenomena occurred while the overall cell voltage remained above 0.3 V. This indicates that only voltage monitoring of fuel cell systems does not contain straightforward information about this type of degradation.

* Corresponding authors.
E-mail addresses: Tim.lochner@bmw.de (T. Lochner), Bandarenka@ph.tum.de (A.S. Bandarenka).

https://doi.org/10.1016/j.apenergy.2019.114291
Received 24 July 2019; Received in revised form 27 November 2019; Accepted 28 November 2019
Available online 21 December 2019

1. Introduction

Renewable energy capacities show an increasing trend in global energy conversion. This causes challenges due to fluctuations in energy production; and a possibility to address these issues is the use of hydrogen as an energy carrier. Therefore, H_2-powered fuel cell electric vehicles (FCEVs) are nowadays becoming an attractive technology for the automotive industry [1–3]. The polymer electrolyte membrane fuel cell (PEMFC) is probably the most relevant type for FCEVs in this context [4,5] due to their high energy conversion efficiency, environmental friendliness, quick refueling time and high power density. However, there are challenges on the way of further commercialization of automotive PEMFCs originating from their limited durability [6,7]. The Department of Energy (DoE) of the United States defines several technical targets for fuel cells listed in Table 1 [8].

Recently, significant progress has been made in achieving reasonable fuel cell system lifetime for automotive applications. However, one of the main remaining tasks thereby is the heterogeneity of degradation of membrane electrode assemblies (MEAs) at the stack level, especially due to transient operation (e.g. load cycling, start-up, shut-down) [9–11].

As discussed by Pollet et al. [12] there are currently only small quantities of commercial FCEVs available on the market, mainly due to availability of the hydrogen infrastructure and due to high costs of fuel cell systems. Nevertheless, there are certain efforts of some automotive companies to invest into fuel cell technology, e.g. the BMW Group announced in 2019 to present a small-series vehicle in 2022 based on a hydrogen fuel cell electric drive system [13]. Some of the main relevant markets to date for FCEVs are the USA, China and Japan.

On a material level, changes in the load influence mainly the cathode and cause Pt dissolution when cycling between certain potentials [14]. For instance, carbon corrosion and catalyst degradation of the cathode is higher under dynamic operation [15,16]. Pei et al. demonstrated that start-ups, shut-downs and transient operation were the dominant sources of the performance decay in vehicle fuel cells, when comparing to the stationary procedures [17]. They found that this was mainly due to poor water management during load cycling, causing flooding and drying of the membrane. This flooding, especially of the anode gas channels, caused fuel starvation. The relevant mechanism was first described by Reiser et al., showing that water blockage of the anode channels leads to carbon corrosion at the cathode catalyst layer [18].

To further analyze these failure mechanisms and to optimize the fuel cell design, in-plane current density and potential distribution of fuel cells during operation were recorded. The technique was initially implemented for PEMFCs in 1997 by Cleghorn et al. [19] Later, Baumgartner et al. [20] correlated the local potentials with the carbon dioxide and carbon monoxide content in the anode and cathode off gases. They found that local fuel starvation caused the local cathode potential to rise leading to carbon corrosion. Furthermore, also high current densities due to poor current density distributions (CDDs) resulted in increased carbon corrosion. Non-uniform potential distributions and CDDs can be triggered by operating the fuel cells using low supply of the oxidant. Increased current densities will thus occur at the gas inlet. In the case of fuel starvation, the non-uniformity is dominated by the local anode potential that is dictating the cathode potential profile [21]. Abbou et al. [22] recently showed that in galvanostatic operation, the anode potential during fuel starvation increased due to a drop in hydrogen partial pressure, causing high overpotentials, and due to the reverse current mechanism. This process occurs mainly at the anode outlet triggering the cathode potentials at the location to increase due to the carbon oxidation and oxygen evolution reactions. In turn, the other areas of the fuel cell need to compensate the low current density at the anode outlet area inducing high current densities at the inlets.

The investigations in aforementioned references took place using lab scale fuel cells with active areas of about 25 cm^2. Yet, it is important to transfer current density measurements also to large area fuel cells that are used in the automotive industry. During normal operation, the oxygen partial pressure, drying and flooding of the MEAs are the key parameters that impact the CDD. High air supply implies high oxygen partial pressures, but at low relative humidity also causes high proton resistance of the membrane. Low hydrogen stoichiometries have little impact on CDDs; only in case of anode flooding the current density at the anode outlet decreases, as described before [23].

Beside the operational strategy, the fuel cell components also impact the CDD. Herden et al. [24,25] used electrode structures with polymers having different equivalent weights to compensate in-plane differences in humidity showing enhanced performance in a wide temperature range. A comparison of oxidant and fuel starvation in automotive size cells was analyzed by Enz et al. [26] finding significantly lower carbon corrosion during air starvation but carbon monoxide and dioxide peaks at cathode and anode exhaust during fuel starvation.

To get closer to real world applications, automotive size fuel cells also need to be tested in representative operational modes. Therefore, several different durability test protocols have been developed, mostly varying the fuel cell load [7]. Gazdzick et al. [11] analyzed dynamic load cycles (DLC) including start-up/shut-down cycles on MEAs with an active area of 25 cm^2. They focused especially on reversible and irreversible degradation mechanisms and found a strong dependence of reversible degradation based on the shut-down strategy. The impact of water and temperature management was in depth analyzed by Sanchez et al. [27] Tests on a 142 cm^2 MEA operated between 60 and 80 °C showed that the cathode humidity was the dominant control value to stabilize the cell performance. Due to lower water uptake of the gas streams at lower cell temperatures, the cells tend to operate more stable at lower operating temperatures. Nandjou et al. [28] performed an extensive research using current density and temperature distribution measurements within a 30-cell stack configuration during load and humidification cycling. Their focus was set on degradation of the bipolar plates (BPP) and membrane during local temperature and humidity cycles based on the New European Driving Cycle.

Recently, DoE analyzed the degradation of Toyota Mirai fuel cells in vehicular operation using their durability test protocols [29]. It has been shown that catalyst particle growth, cathode catalyst layer compaction and membrane thinning after 3000 h of real driving are negligible. However, the Mirai fuel cells were not stable when using the DoE test protocol. After 5000 cycles, the electrochemical surface area (ECSA) loss was 60%, particle size increased by more than 10% and only little performance remained. The difference between the real driving and DoE test protocol mainly originated from mitigation strategies employed at system level to avoid degradation [29]. During automotive operation, gas pressures, stoichiometries, humidity, cell current and temperature are varying simultaneously. Increased outlet pressures lead to decreased pressure losses along the flow channels and thereby to lower water removal capability. Increased current densities lead to higher temperatures due to increased reaction enthalpy [30] and can trigger more homogeneous temperature distributions due to increased gas flows [31]. Low inlet gas humidification might lead to more non-uniform temperature distributions due to inhomogeneous membrane humidification [32]. These examples of interactions

Table 1
Some technical targets for membrane electrode assemblies for transport applications as defined by the US Department of Energy [8].

Characteristic	Units	2020 Targets (DoE)
Durability with cycling	h	5000
Performance @ 0.8 V	mA/cm^2	300
Performance @ rated power (150 kPa_{abs})	mW/cm^2	1000

between local temperature, current and humidity show that it is incremental for real-word applications to investigate realistic drive cycles that cycle all relevant operational parameters simultaneously. Most publications focus on test protocols analyzing the impact of isolated operational parameters [7,33] even though a strong interaction between the operational parameters takes place as modeled by Chen et al. [34]. The here presented work investigates coupled phenomena using a real-world test protocol that cycles the most relevant operational parameters simultaneous.

The objective of this work is to investigate and compare the damaging impact of different operational parameters with respect to the overall cell performance, degradation mechanisms and identification of most harmful operation conditions for automotive size PEMFCs. The implemented parameter sets are thereby extracted from customer driving profiles, including high load operation as well as cycling of gas pressures, humidity, load, stoichiometry and cell temperature. The operational conditions compared to other cycling papers were adjusted to required automotive parameter ranges. Therefore, the parameter range was extended up to 2.0 A cm^{-2}, 90 °C cell temperature, 175 kPa operating pressure (absolute) and down to the cathode stoichiometries of 1.4 [11,7,27,28]. Ex-situ investigations were used to analyze the impact on component degradation and correlated to operational parameters via CDD measurements. Degradation of electrodes and membrane are put into perspective of flow field design and operational strategy.

2. Experimental

2.1. Cell design

The cell set up is illustrated in Fig. 1 and comprises of two metallic bipolar plates (BPPs), two gas diffusion layers/micro porous layers (GDLs/MPLs), one catalyst coated membrane (CCM), two gold plated copper end plates, one current scan shunt (CSS), and two compression plates. The commercial GDL was obtained by SGL Carbon SE. On the anode side the type 29 BC (thickness 235 µm) while on the cathode side a special designed GDL by SGL Carbon SE 22 BB (thickness 220 µm) were used. The catalyst coated membrane was provided by Johnson Matthey Fuel Cells. The catalyst material was pure platinum on anode and cathode. The catalyst loadings on anode and cathode were 0.05 and 0.3 mg/cm^2, respectively. The anode and cathode catalyst layer thicknesses were approximately 3 and 8 µm, respectively. The thickness of the polymer membrane was 15 µm. Filtered air and hydrogen with a purity of 99.999% were used to operate the fuel cell.

2.2. Current density distribution measurements

A commercial CSS sensor plate provided by S++ Simulation Services was used to measure the CDD. A detailed description is provided by Kraume [35]. The CSS consisted of 17 × 32 segments with a total area of 287.9 cm^2. The active area of the CCM was similar and therefore all segments of the CSS were considered during data analysis. A schematic of the cell set up is illustrated in Fig. 1A. The CSS was placed between the cathode BPP and the endplate. On both sides of the CSS active area two graphite foils provided by SGL Carbon SE were attached to guarantee electrical contact between the CSS and the BPPs. A BPP with closed gas and cooling channels was used to seal the CSS. To provide electrical conductivity another graphite foil was placed between BPP and end plate. Homogeneous pressure distribution within the active area of the cell was obtained by adding an aluminum pressure plate. Between graphite foil and pressure plate, an isolation plate is placed to electrically isolate the surrounding from the cathode cell potential. Pressure distribution maps were recorded using Fujifilms to guarantee homogenous contact of the CSS to the cell.

The CSS is meant to measure the current density distribution of the CCM. As illustrated in Fig. 1A, a bipolar plate and a graphite foil separate the CSS from the MEA. They do have a certain in-plane electrical conduction that influences the current density distribution measured at the CSS. The current density within the CCM based on CSS measurements can be determined using a numerical model that includes the electrical conductivities of the layers between CCM and CSS. In this work the numerical approach similar to Haase et al. [36] and Herden et al. [24] based on a finite-volume framework [37] was applied.

2.3. Bipolar plate design

The automotive BPPs used in this work were provided by DANA (Reinz-Dichtungs GmbH). The plates were made from stainless steel with a carbon coating on top of the land areas to decrease contact resistance between GDL and BPP. An illustration of the anode plane of the BPP is shown in Fig. 1B. The BPP consisted of two monopolar plates with anode and cathode flow channels that were welded together. The section between the two monopolar plates built channels for water used as coolant. The cell was always operated in counter flow regime. Beaded gaskets were used to seal the cell. A straight flow was realized at anode and cathode. The gas distribution zones (see Fig. 1B) are designed to gain a homogeneous gas distribution among the flow channels within the active area of the cell.

2.4. Degradation tests

On-road customer data of conventional cars were taken to determine the power sequences requested by the driver. The power sequences were used as input parameter for a fuel cell system simulation tool. The simulation tool provided the corresponding operating points for the fuel cell stack itself. Out of these, seven different operational parameter sets were defined to represent states that occur during the automotive system operation. These sets contain different values for the following operational parameters:

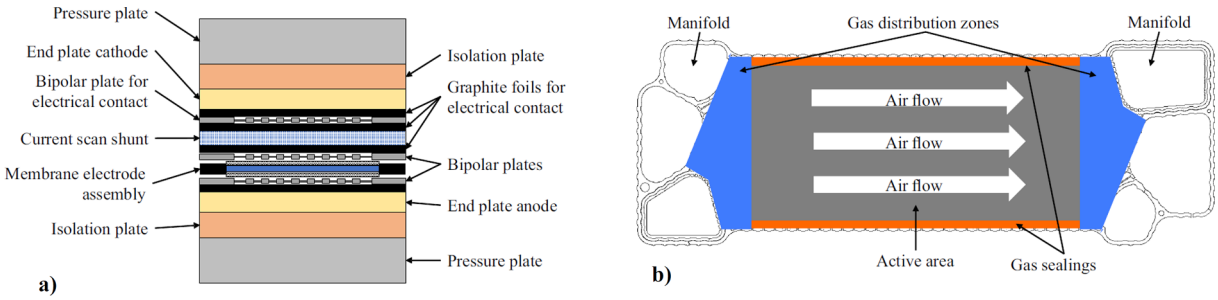

Fig. 1. Cell hardware used to operate the fuel cell. (A) Schematics of the cell set up (B) BPP with the cathode flow field (straight flow channels). The white arrows in the middle of the flow field indicate the flow direction of air.

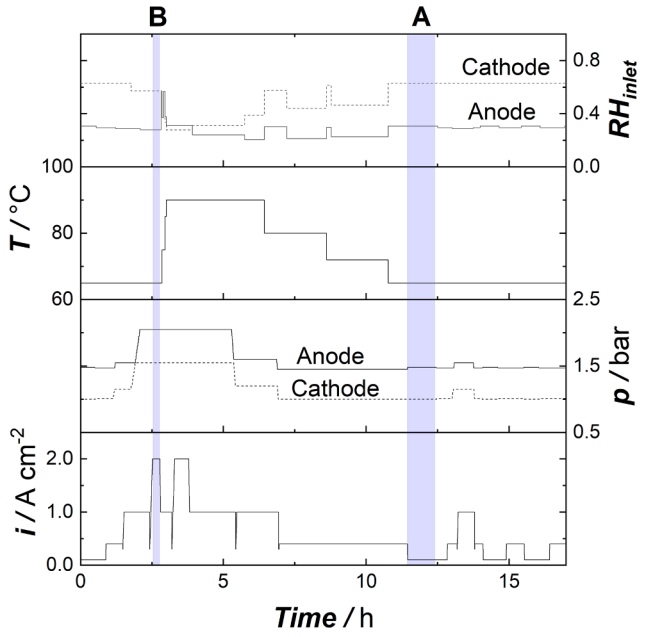

Fig. 2. Operational parameters during one cycle of the testing protocol. The upper figure shows the average relative humidity (RH) at the inlets of anode and cathode compartment as a function of time. The figure below shows the cell temperature variations. The next figure illustrates the gas pressures changes at the outlets of anode and cathode. The bottom graph shows the load current, *i*, during the tests. The labels A and B at the top of the graph designate two specific operational parameter sets.

- Current density
- Coolant inlet temperature
- Anode and cathode inlet gas humidification
- Anode and cathode stoichiometry
- Anode and cathode outlet gas pressure

For the single cell test described here, operational parameters of a cell located in the middle of an automotive fuel cell stack are taken. The sequence of the operational parameter sets is illustrated in Fig. 2. The stoichiometries vary between 1.25 and 1.38 at the anode side. At the cathode, the stoichiometry varies between 1.40 and 1.60. Humidification of the electrodes was controlled using a bubbler-based humidification system. The testing protocol was performed using automated test scripts. To prevent cell damages, safety points were approached when the cell voltage dropped below 0.3 V for longer than 1 s. Within the safety point, the cell was switched from galvanostatic to potentiostatic operation with the voltage of 0.75 V. The volume flows of anode and cathode were controlled by stoichiometry. To avoid media starvation, minimum gas flows of 1 and 2.5 Nl min^{-1} were defined for the anode and the cathode, respectively.

To minimize influences due to inhomogeneous temperature distribution a coolant flow rate of 1.5 Nl min^{-1} was used. Thereby, the temperature spread from cathode inlet to outlet is 1.5 K and remained constant throughout the whole experiment.

Scanning electron microscopy (SEM) coupled with energy dispersive X-ray spectroscopy (EDX) is used to characterize the catalyst layer at EoT. As the BoL reference, the catalyst layer of the same MEA type and batch was analyzed. SEM backscatter images were recorded using a Hitachi TM3030 Plus microscope.

2.5. Simulation

A computational fluid dynamic (CFD) half-cell model for the anode was built-up in order to design a flow field with a homogeneous mass flow distribution of the gas flow channels. This is achieved by introducing a gas distribution zone (Fig. 1 right) that directs the gases from the manifolds to the active area of the cell; the CFD approach was published by Enz et al. [38]. The half-cell geometry consisted of the flow field, GDL, MPL and electrode as fluid zones. A homogeneous CDD was assumed using volumetric sink and source terms inside the electrode. Additionally, only the gas phase was considered in the model and the mean temperature of the cell was applied as the isothermal condition. Geometric and material properties of the experimentally used components were taken into account within the simulation. The operational parameter set A (see Fig. 2) summarizes the boundary conditions for the simulation. The mass flows at the anode media inlet at the stoichiometry specified in Fig. 2 are listed in Table 2. The external humidification is taken into account in the gas mixture settings at the cell inlet. The water balance of the anode compartment was considered using source and sink terms related to a back diffusion flux and electro osmotic drag. An overview of the boundary conditions is listed in Table 2.

Table 2
The boundary conditions used in the CFD half-cell model.

Operational parameters		
	Current density / A cm^{-2}	0.1
	Cell temperature/K	330
	Operational pressure/kPa	148
Mass flow at inlet		
	Mass flow/kg s^{-1}	$1.62 \cdot 10^{-6}$
	Temperature/K	330
	H_2 mole ratio	0.807
	N_2 mole ratio	0.128
	H_2O mole ratio	0.065

3. Results

3.1. In-situ diagnostics

The cell was operated for an accumulated time of about 300 h accomplishing 20 cycles. During testing, there were 2 interrupts after 130 and 200 h of testing time. In both cases the cell voltage increased compared to the pre-shutdown when restarting the cell again. This is commonly explained by recovery effects of the catalyst layer. The startup protocol followed a procedure optimized to maintain a homogeneous CDD. The CDD at BoL is illustrated in Fig. 3C.

Fig. 3C–E show the CDD maps at different testing times. For comparability, the CDD maps correspond to the same operational parameter set. In this case, parameter set A, as described beforehand in Fig. 2, is represented. Parameter set A was chosen as reference set since the inhomogeneous behavior is most pronounced at low current densities.

At the BoL, the current densities closer to the anode inlet ($H_{2,in}$) are higher than the mean current density. Segments closer to the anode outlet ($H_{2,out}$) show currents lower than the mean current. During testing, currents close to the anode inlet increase while those close to anode outlet decrease. This is in more detail illustrated in Fig. 3A. Fig. 3A shows the trend of two segments, one of them close to anode inlet (segment 2) and one close to the anode outlet (segment 31). The trends of segments 2 and 31 are representative for segments close to anode inlet and outlet, respectively. The current density in segment 2 is rather linearly increasing over time. The current density in segment 31 decreases linearly within the first 200 h, afterwards it decreases exponentially. Fig. 3E shows the CDD after about 300 h of operation. Negative currents occur in parameter set A (Fig. 2) at positions close to the anode outlet. This phenomenon is only observed at current densities below 0.2 A cm^{-2} and when operating in potentiostatic mode at 0.75 V. The trend of increasing current spread between the anode inlet and outlet can be seen in all parameter sets. Nevertheless, it is more pronounced at the parameter sets with current densities below 0.2 A cm^{-2}.

Fig. 3B illustrates the voltage within the operational parameter set

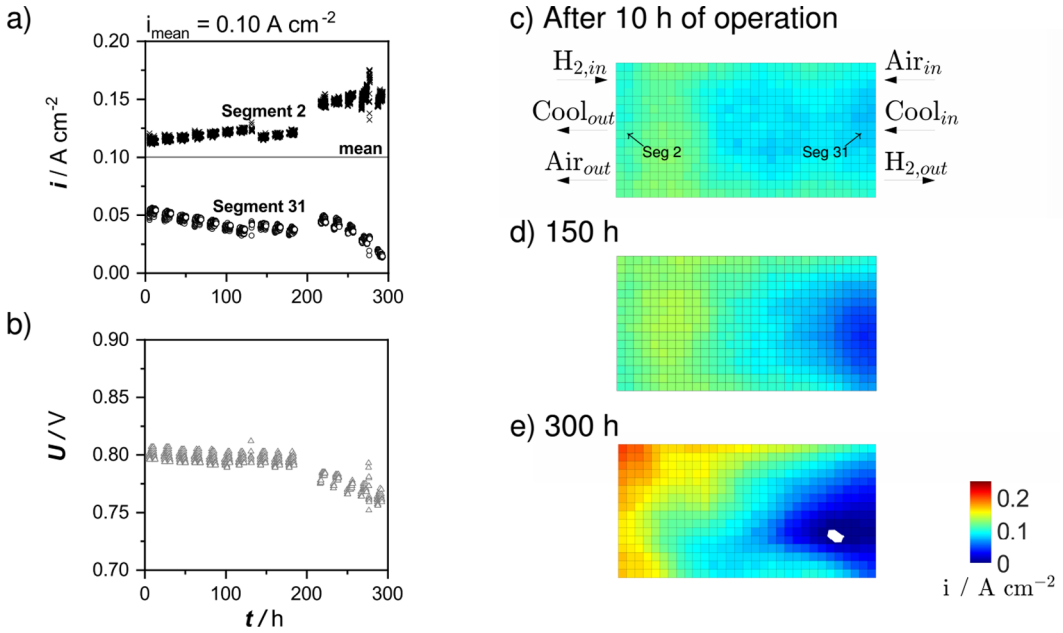

Fig. 3. Experimentally measured current density distribution (CDD) at an average current of 0.1 A cm^{-2} (corresponding to parameter set A in Fig. 2). (A) Current densities at segments 2 and 31 (see Fig. 3C for segment location) and (B) the corresponding overall cell voltage. (C–E) current density distribution maps based on current scan shunt measurements after 10 h (cycle 1), 150 h (cycle 9) and 300 h (cycle 14) of operation. Within the current density distribution maps the values below 0 A cm^{-2} are displayed using white color. The flow directions of air, hydrogen and coolant are indicated on (C) and are similar for all three maps. The color bar (right, bottom) applies for all three maps.

A. Within the first 200 h of operation the voltage is decreasing with a rate of 0.042 mV h^{-1}. Between 200 and 300 h, the slope increases to 0.25 mV h^{-1}. With increasing testing time, the voltage decreases while the spread in current density over the MEA also increases. It is emphasized that the overall cell voltage stays above 0.3 V throughout the whole experiment. Therefore, degradation effects due to global cell voltage reversal do not play a role within this analysis.

The CDDs in Fig. 3 are always correlated to the partial pressure of hydrogen. Due to the high overpotential of the oxygen reduction reaction compared to the hydrogen oxidation reaction, the illustrated trends were not expected. To further investigate the impact of the anode conditions on the CDD a hydrogen stoichiometry variation was carried out as illustrated in Fig. 4. When ramping up the stoichiometry from 1.4 to 1.8 the overall cell voltage increases from 0.4 to 0.48 V. At a hydrogen stoichiometry of 1.4 the current density close to the anode inlet (Fig. 4A) is close to 0 A cm^{-2}. When increasing the hydrogen stoichiometry to 1.5 and 1.8 the current density distribution gets more homogeneous and the region with low current densities disappears. At the highest stoichiometry the CDD follows the partial pressure of oxygen as expected.

Beside CDD maps also the temperature distribution was recorded during testing. The average temperature increases by 0.4 °C while the temperature spread over the the MEA stays constant throughout the whole experiment at 1.5 K. Therefore, the impact of inhomogeneous membrane hydration on the CDD is assumed to be low.

3.2. Ex-situ diagnostics

Fig. 5B shows a photograph of the cathode CCM after about 300 h of operation. There are three areas that show a different surface structure. The areas close to the ports are rougher than the area in the center of the CCM. The area marked with yellow borders correspond to the area that showed MPL deposits on top of the CCM as well as CCM crack formation. Fig. 5A shows corresponding SEM cross section images of the cathode electrode (close to the membrane interface) at the anode inlet in comparison to the cathode electrode layer close to the anode outlet. The typical porous structure of the cathode is still visible within the cathode layer close to the anode inlet. The cross section close to the anode outlet shows a collapsed cathode electrode structure indicating carbon corrosion within this area. The yellow line in Fig. 5A marks the area where these effects could be observed. The cathode catalyst layer thickness close to the anode outlet is thereby decreased to 4.8 µm, compared to 6.8 µm at the anode inlet.

A CDD map close to the EoT recorded during parameter set A is shown in Fig. 5D. The region that shows low and negative current densities during operation also shows the strongest catalyst degradation in ex situ diagnostics. SEM images of the anode catalyst layer within the areas with low current densities did not show noticeable degradation.

3.3. Results of numerical simulations

Fig. 5C illustrates the results of numerical simulations for the relative humidity within the anode electrode layer. The simulated parameter set corresponds to parameter set A in Fig. 2. The maximum relative humidity is close to the anode outlet with ca. 163%. The simulation shows an increase of relative humidity from the anode inlet towards the anode outlet. This indicates that close to the anode outlet liquid water is present within the anode electrode. The general trend as illustrated in Fig. 5C can also be found in simulations with higher current densities.

4. Discussion

The CDD was shown to be mainly dependent on the hydrogen volume flow during the experiment. It is suggested that the anode electrode flooding dominates the CDD. Simulation results confirm the assumption on the electrode flooding at the beginning of life. This might be caused by low pressure losses within the anode flow field due to the straight channel flow configuration. To investigate this hypothesis, the pressure at anode inlet to outlet within parameter set B (Fig. 2) was analyzed. An increase in pressure drop by about 60 mbar was observed within this parameter set. Fig. 5 illustrates that the areas with high anode electrode relative humidity correspond to the low current density regions during operation. Additionally, the cathode within this area

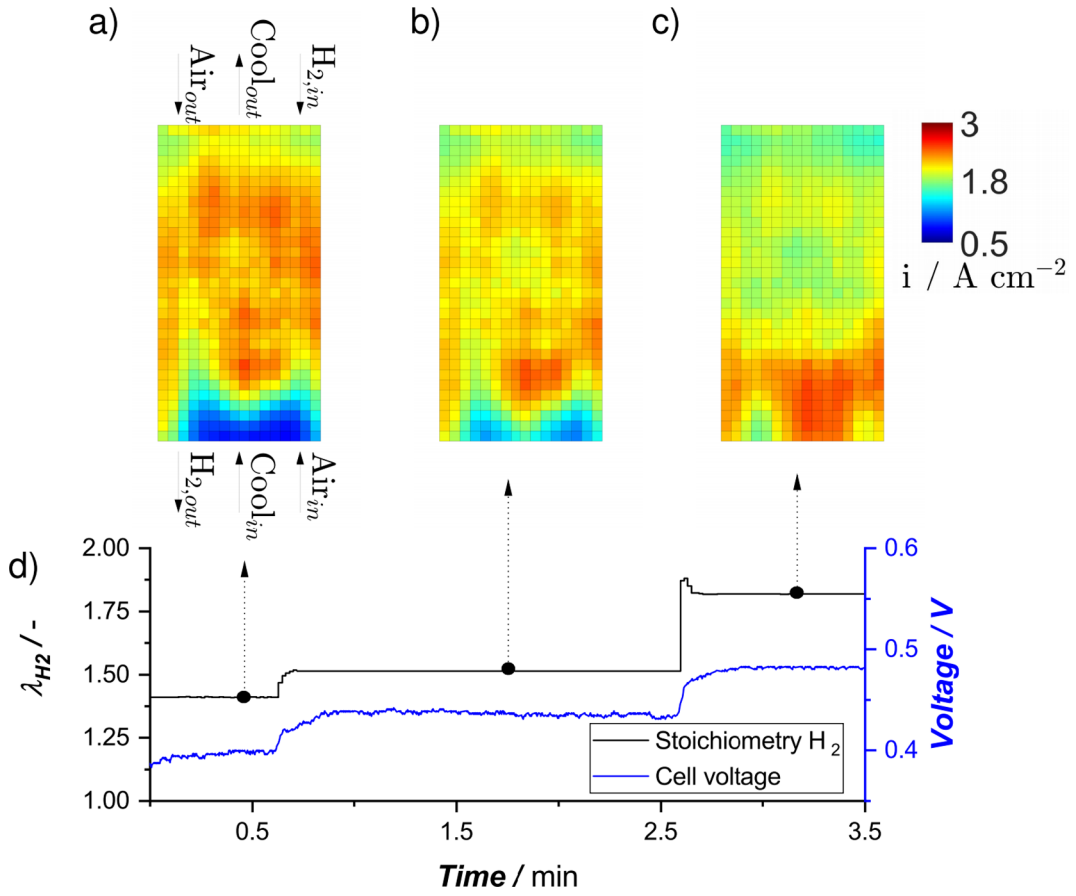

Fig. 4. (A-D) Anode volume flow variation including current density distribution maps based on current scan shunt measurements. (D) Anode volume flow variation over time and corresponding overall cell voltage. All other operational parameters are constant during the variation. (A, B, C) Corresponding current density distribution maps. The color bar on the right corresponds to all three current density distribution maps.

was found to be stronger corroded than in other areas of the CCM. Negative currents were found within the anode outlet region. As described by Reiser et al. [18] local fuel starvation causes corrosion of the cathode electrode within this region. Therefore, flooding of the anode electrode layer is assumed to be the dominant degradation mechanism within this experiment. As previously shown in Fig. 4, the current density spread decreases with increasing hydrogen stoichiometry. This indicates that the higher gas volume flows at prevent anode flooding. Therefore, operation at low anode volume flows (low current densities and potentiostatic modes) are mainly contributing to local anode fuel starvation as is well known in literature. The effect of the local anode starvation gets especially dominant, when jumping from high current densities with high water production to low current densities, where the hydrogen gas flow has a low water discharge capacity.

Fig. 3C–E disclose that the effect of anode flooding increases over time. It is hypothesized that flooding at the anode outlet features a "self-energizing" mechanism: The catalyst layer at the area prone to fuel starvation shows more cracks than other areas due to carbon corrosion. As described by Mehmood et al. [39] electrode flooding is supported by increasing crack formation within the electrode layer. Therefore, flooding of the anode electrode at BoL causes higher water contents at the cathode electrode layer in regions close to the anode outlet. This in turn leads to high water contents at the anode electrode layer due to diffusion of water through the polymer membrane. It is likely that the increased amount of liquid water within the anode electrode causes a rise in liquid water within the GDL and flow field. Therefore, the channel diameter within the flow field channels that are located within flooded areas is decreased and causes increased backpressures as observed in this study. Due to the straight flow alignment of the channels this causes the hydrogen flow to flow along the edges of the flow field. Therefore, current densities are higher on the edges of the flow field close to the anode outlet (e.g. Fig. 5C) while fuel starvation is promoted in the middle. The area subject to this degradation process is increasing with operational time. The optimization of the flow field and operational strategy especially at low hydrogen flow rates plays a key role to avoid inclined flooding of the anode compartment with increasing operational time.

5. Conclusions

In this study, an automotive size single cell was operated under automotive operational parameter sets. The cell was in-situ characterized using a current scan shunt. The current density distribution was dominated by the partial pressure of hydrogen due to flooding of the anode catalyst layer close to the anode outlet especially when jumping from high to low current densities. This led to fuel starvation within the anode outlet region. The development of flooding within the anode electrode layer was analyzed by evaluating the current density distribution maps. The flooded area increased over time. During testing also the pressure drop along the anode flow field increased. A mechanism that indicates that flooding of the anode catalyst layer is a self-energizing effect that leads to failure of the cell is proposed. This is mainly impacted by crack formation of the cathode catalyst layer within these regions that could be shown by SEM analysis. Decreased pressure drops of the straight flow channels reduce the capability of the flow field to effectively remove liquid water. Therefore, optimization of the flow field plays a key role in avoiding flooding of the anode. In addition, the use of a CSS measurement allowed an in-situ diagnostic tool to evaluate different operational strategies with respect to fuel starvation.

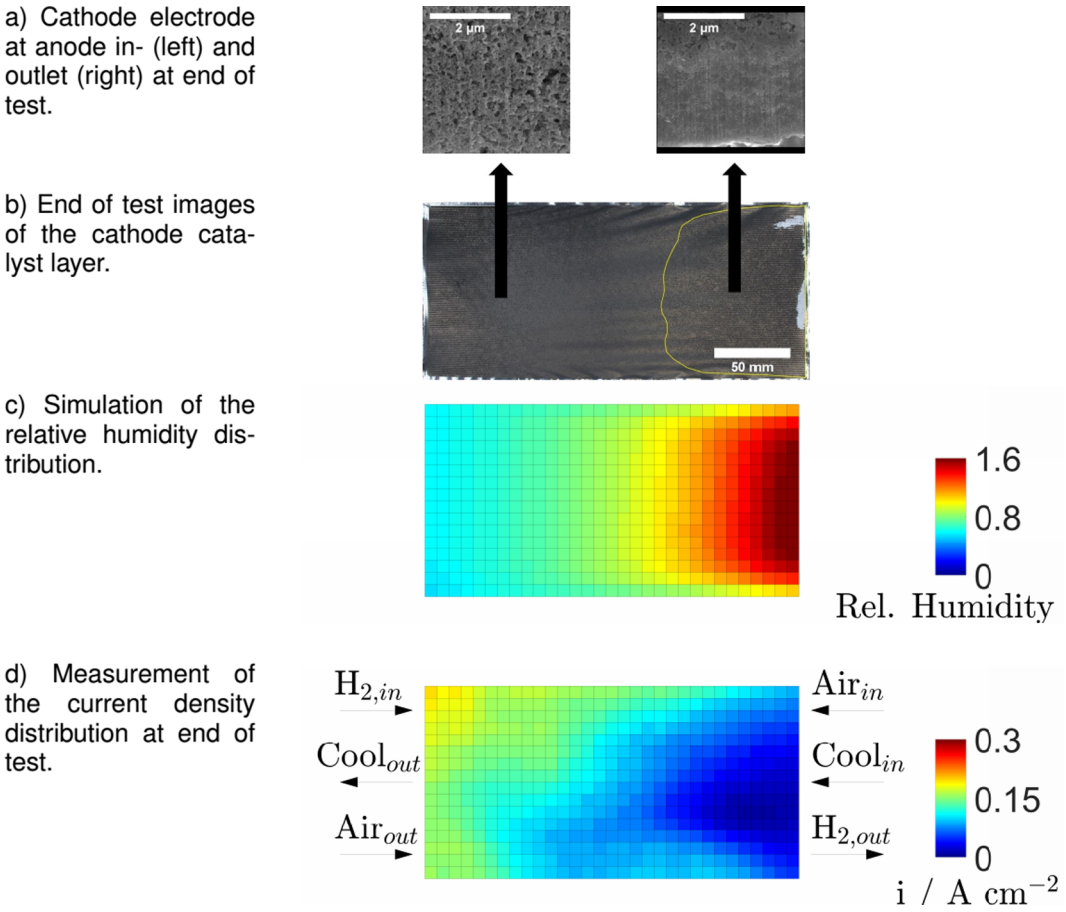

Fig. 5. Distribution maps at parameter set A shown in Fig. 2. (A) SEM cross section images of the cathode electrode. The location of the specimens is indicated by two black arrows related to Fig. 5B. A backscatter detector was used for these illustrations. (B) Photograph of the cathode microporous layer at the end of test (EoT). (C) Simulated relative humidity distribution at the anode electrode layer. (D) Current density distributions during operation close to EoT. The media flow directions indicated in figure (D) are similar for all three images.

CRediT authorship contribution statement

Tim Lochner: Data curation, Formal analysis, Investigation, Writing - original draft, Writing - review & editing. **Laurens Hallitzky:** Data curation, Formal analysis, Investigation, Writing - original draft, Writing - review & editing. **Markus Perchthaler:** Conceptualization, Funding acquisition, Project administration, Resources, Supervision, Writing - original draft, Writing - review & editing. **Michael Obermaier:** Data curation, Formal analysis, Investigation, Writing - original draft, Writing - review & editing. **Jarek Sabawa:** Data curation, Formal analysis, Investigation, Writing - original draft, Writing - review & editing. **Simon Enz:** Data curation, Formal analysis, Investigation, Writing - original draft, Writing - review & editing. **Aliaksandr S. Bandarenka:** Supervision, Writing - original draft, Writing - review & editing.

Declaration of Competing Interest

The authors declare that they have no known competing financial interests or personal relationships that could have appeared to influence the work reported in this paper.

Acknowledgment

The authors would like to thank BMW Technology Material and Process Analysis (TWA) for performing the ex-situ analytics. Furthermore, we thank Savo Asanin for supporting the data processing and illustration. The project (INSPIRE) has received funding from the Fuel Cells and Hydrogen 2 Joint Undertaking under grant agreement No 700127. This Joint Undertaking receives support from the European Union's Horizon 2020 research and innovation programme, Hydrogen Europe and Hydrogen Europe Research.

References

[1] Henning H-M, Palzer A. Energiesystem Deutschland 2050. Fraunhofer Institut für Solare Energiesysteme ISE. https://www.ise.fraunhofer.de/content/dam/ise/de/documents/publications/studies/Fraunhofer-ISE_Energiesystem-Deutschland-2050.pdf (Access: April 2019).
[2] Konno N, Mizuno S, Nakaji H, Ishikawa Y. Development of compact and high-performance fuel cell stack. SAE Int J Alternative Powertrains 2015;4:123–9. https://doi.org/10.4271/2015-01-1175.
[3] Li Q, Aili D, Hjuler HA, Jensen JO, editors. High temperature polymer electrolyte membrane fuel cells. Cham Heidelberg New York Dordrecht London: Springer; 2016. p. 545.
[4] Debe MK. Electrocatalyst approaches and challenges for automotive fuel cells. Nature 2012;486:43–51.
[5] Fouqet N, Doulet C, Nouillant C, Dauphin-Tanguy G, Ould-Bouamama B. Model based PEM fuel cell state-of-health monitoring via ac impedance measurements. J Power Sources 2006;159:905–13. https://doi.org/10.1016/j.jpowsour.2005.11.035.
[6] Mayrhofer KJJ, Meier JC, Ashton SJ, Wiberg GKH, Kraus F, Hanzlik M, et al. Fuel cell catalyst degradation on the nanoscale. Electrochem Commun 2008;10:1144–7. https://doi.org/10.1016/j.elecom.2008.05.032.
[7] Chen H, Song Z, Zhao X, Zhang T, Pei P, Liang C. A review of durability test protocols of the proton exchange membrane fuel cells for vehicle. Appl Energy 2018;224:289–99. https://doi.org/10.1016/j.apenergy.2018.04.050.
[8] Department of Energy. DOE Technical Targets for Polymer Electrolyte Membrane Fuel Cell Components. https://www.energy.gov/eere/fuelcells/doe-technical-targets-polymer-electrolyte-membrane-fuel-cell-components (Access: October 2019).
[9] Wang G, Yu Y, Chunli Gong HL, Xiaohua Wang SW, Tu Z. Progress on design and

development of polymer electrolyte membrane fuel cell systems for vehicle applications: a review. Fuel Process Technol 2017;179:203–28. https://doi.org/10.1016/j.fuproc.2018.06.013.
[10] Du J, Ouyang M, Chen J. Prospects for Chinese electric vehicle technologies in 2016–2020: ambition and rationality. Energy 2017;120:584–96. https://doi.org/10.1016/j.energy.2016.11.114.
[11] Gazdzick P, Mitzel J, Garcia Sanchez D, Schulze M, Friedrich KA. Evaluation of reversible and irreversible degradation rates of polymer electrolyte membrane fuel cells tested in automotive conditions. J Power Sources 2016;327:86–95. https://doi.org/10.1016/j.jpowsour.2016.07.049.
[12] Pollet BG, Kocha SS, Staffell I. Current status of automotive fuel cells for sustainable transport. Curr Opin Electrochem 2019;16:90–5. https://doi.org/10.1016/j.coelec.2019.04.021.
[13] BMW Group. The BMW i Hydrogen NEXT at the IAA Cars 2019. BMW Group Corporate Communications. https://www.press.bmwgroup.com/global/article/detail/T0300507EN/the-bmw-i-hydrogen-next-at-the-iaa-cars-2019. (Access: October 2019).
[14] Borup R, Meyers J, Pivovar B, Kim YS, Mukundan R, Garland N, Myers D, Wilson M, Garzon F, Wood D, Zelenay P, More K, Stroh K, Zawodzinski T, Boncella J, McGrath JE, Inaba M, Miyatake K, Hori M, Ota K, Ogumi Z, Miyata S, Nishikata A, Siroma Z, Uchimoto Y, Yasuda K, Kimjima K-C, Iwashita N. Scientific aspects of polymer electrolyte fuel cell durability and degradation. Chem. Rev. 2007;107:3904–51. https://doi.org/10.1021/cr050182l.
[15] Maass S, Finsterwalder F, Frank G, Hartmann R, Merten C. Carbon support oxidation in PEM fuel cell cathodes. J Power Sources 2008;176:444–51. https://doi.org/10.1016/j.jpowsour.2007.08.053.
[16] Wang G, Huang F, Yu Y, Wen S, Tu Z. Degradation behavior of a proton exchange membrane fuel cell stack under dynamic cycles between idling and rated condition. Int J Hydrogen Energy 2018;43:4471–81. https://doi.org/10.1016/j.ijhydene.2018.01.020.
[17] Pei P, Chen H. Main factors affecting the lifetime of Proton Exchange Membrane fuel cells in vehicle applications:a review. Appl Energy 2014;125:60–75. https://doi.org/10.1016/j.apenergy.2014.03.048.
[18] Reiser CA, Bregolia L, Patterson TW, Yi JS, Yangb JD, Perry ML, et al. A reverse-current decay mechanism for fuel cells. Electrochem Solid-State Lett 2005;8:273–6. https://doi.org/10.1149/1.1896466.
[19] Cleghorn SJC, Derouin CR, Wilson MS, Gottesfeld S. A printed circuit board approach to measuring current distribution in a fuel cell. J Appl Electrochem 1998;28:663–72. https://doi.org/10.1023/A:1003206513954.
[20] Baumgartner WR, Parz P, Fraser SD, Wallnöfer SD, Hacker V. Polarization study of a PEMFC with four reference electrodes at hydrogen starvation conditions. J Power Sources 2008;182:413–21. https://doi.org/10.1016/j.jpowsour.2008.01.001.
[21] Manokaran A, Pushpavanam S, Sridhar P. Dynamics of anode-cathode interaction in a polymer electrolyte fuel cell revealed by simultaneous current and potential distribution measurements under local reactant-starvation conditions. J Appl Electrochem 2015;45:353–63. https://doi.org/10.1007/s10800-015-0800-9.
[22] Abbou S, Dillet J, Maranzana G, Didierjean S, Lottin O. Local potential evolutions during proton exchange membrane fuel cell operation with dead-ended anode – Part I: impact of water diffusion and nitrogen crossover. J Power Sources 2017;340:337–46. https://doi.org/10.1016/j.jpowsour.2016.11.079.
[23] Büchi FN, Geiger AB, Neto RB. Dependence of current distribution on water management in PEFC of technical size. J Power Sources 2005;145:62–7. https://doi.org/10.1016/j.jpowsour.2004.12.039.
[24] Herden S, Riewald F, Hirschfeld JA, Perchthaler M. In-plane structuring of proton exchange membrane fuel cell cathodes: Effect of ionomer equivalent weight structuring on performance and current density distribution. J Power Sources 2017;355:36–43. https://doi.org/10.1016/j.jpowsour.2017.04.051.
[25] Herden S, Hirschfeld JA, Lohri C, Perchthaler M, Haase S. Ionomer equivalent weight structuring in the cathode catalyst layer of automotive fuel cells: effect on performance, current density distribution and electrochemical impedance spectra. J Power Sources 2017;364:449–57. https://doi.org/10.1016/j.jpowsour.2017.08.057.
[26] Enz S, Dao TA, Messerschmidt M, Scholta J. Investigation of degradation effects in polymer electrolyte fuel cells under automotive-related operating conditions. J Power Sources 2015;274:521–35. https://doi.org/10.1016/j.jpowsour.2014.10.127.
[27] Sanchez DG, Ruiua T, Friedricha KA, Sanchez-Monrealb J, Verab M. Analysis of the influence of temperature and gas humidity on the performance stability of polymer electrolyte membrane fuel cells. J Electrochem Soc 2016;163:150–9. https://doi.org/10.1149/2.0071603jes.
[28] Nandjou F, Poirot-Crouvezier J-P, Chandesris M, Blachot J-F, Bonnaud C, Bultel Y. Impact of heat and water management on proton exchange membrane fuel cells degradation in automotive application. J Power Sources 2016;326:182–92. https://doi.org/10.1016/j.jpowsour.2016.07.004.
[29] Borup R, More K, Weber A. FC135: FC-PAD: Fuel Cell Performance and Durability Consortium; 2018, https://www.hydrogen.energy.gov/pdfs/review18/fc135_borup_2018_o.pdf (Access: April 2019).
[30] Shao H, Qiu D, Peng L, Yi P, Lai X. In-situ measurement of temperature and humidity distribution in gas channels for commercial-size proton exchange membrane fuel cells. J Power Sources 2019;412:717–24. https://doi.org/10.1016/j.jpowsour.2018.12.008.
[31] Guo H, Wang MH, Liu JX, Nie ZH, Ye F, Ma CF. Temperature distribution on anodic surface of membrane electrode assembly in proton exchange membrane fuel cell with interdigitated flow bed. J Power Sources 2015;273:775–83. https://doi.org/10.1016/j.jpowsour.2014.09.159.
[32] Shimoi R, Masuda M, Fushinobu K, Kozawa Y, Okazaki K. Visualization of the membrane temperature field of a polymer electrolyte fuel cell. J. Energy Resour. Technol. 2004;126:258–61. https://doi.org/10.1115/1.1811119.
[33] Zhao J, Li X. A review of polymer electrolyte membrane fuel cell durability for vehicular applications: degradation modes and experimental techniques. Energy Convers Manage 2019;199. https://doi.org/10.1016/j.enconman.2019.112022.
[34] Chen D, Singh S, Gao L, Garg A, Fan Z, Wang C-T. A coupled and interactive influence of operational parameters for optimizing power output of cleaner energy production systems under uncertain conditions. Int J Energy Res Short Commun 2019;43.
[35] Kraume R. S++ Simulation Services; 2007. URL, http://www.splusplus.com/ (Access: April 2019).
[36] Haase S, Moser M, Hirschfeld JA, Jozwiak K. Current density and catalyst coated membrane resistance distribution of hydro-formed metallic bipolar plate fuel cell short stack with 250 cm^2 active area. J Power Sources 2016;301:251–60. https://doi.org/10.1016/j.jpowsour.2015.09.118.
[37] Hirschfeld JA, Lustfeld H, Reißel M, Steffen B. A novel scheme for precise diagnostics and effective stabilization of currents in a fuel cell stack. Int J Energy Res 2010;34:293–302.
[38] Enz S, Klages M, Bergbreiter C, Messerschmidt M, Markötter H, Kardjilov N, et al. Investigation on dynamic water transport of PEFCs combining neutron radiography and CFD simulation. ECS Trans 2013;51:215–26. https://doi.org/10.1149/05101.0215ecst.
[39] Mehmood A, An MG, Ha HY. Physical degradation of cathode catalyst layer: a major contributor to accelerated water flooding in long-term operation of DMFCs. Appl Energy 2014;129:346–53. https://doi.org/10.1016/j.apenergy.2014.05.016.